SCIENTIFIC REP🞑RTS

Hydrogen and nitrogen codoping of anatase TiO$_2$ for efficiency enhancement in organic solar cells

Maria Vasilopoulou[1], Nikolaos Kelaidis[2], Ermioni Polydorou[1,3], Anastasia Soultati[1], Dimitris Davazoglou[1], Panagiotis Argitis[1], Giorgos Papadimitropoulos[1], Dimitris Tsikritzis[4], Stella Kennou[4], Florian Auras[5], Dimitra G. Georgiadou[1,6], Stavros-Richard G. Christopoulos[2] & Alexander Chroneos[2,7]

TiO$_2$ has high chemical stability, strong catalytic activity and is an electron transport material in organic solar cells. However, the presence of trap states near the band edges of TiO$_2$ arising from defects at grain boundaries significantly affects the efficiency of organic solar cells. To become an efficient electron transport material for organic photovoltaics and related devices, such as perovskite solar cells and photocatalytic devices, it is important to tailor its band edges via doping. Nitrogen p-type doping has attracted considerable attention in enhancing the photocatalytic efficiency of TiO$_2$ under visible light irradiation while hydrogen n-type doping increases its electron conductivity. DFT calculations in TiO$_2$ provide evidence that nitrogen and hydrogen can be incorporated in interstitial sites and possibly form N_iH_i, N_iH_O and $N_{Ti}H_i$ defects. The experimental results indicate that N_iH_i defects are most likely formed and these defects do not introduce deep level states. Furthermore, we show that the efficiency of P3HT:IC$_{60}$BA-based organic photovoltaic devices is enhanced when using hydrogen-doping and nitrogen/hydrogen codoping of TiO$_2$, both boosting the material n-type conductivity, with maximum power conversion efficiency reaching values of 6.51% and 6.58%, respectively, which are much higher than those of the cells with the as-deposited (4.87%) and nitrogen-doped TiO$_2$ (4.46%).

Metal oxides such as titanium dioxide (TiO$_2$) have been intensively investigated for more than four decades because of their strong catalytic activity, high chemical stability and long lifetime of photon generated carriers[1–10]. Anatase exhibits the highest photocatalytic activity of the polymorphs of TiO$_2$, however, it is constrained to the limited ultraviolet range (UV irradiation is only 5%) of the solar spectrum due to its large band gap (3.2 eV)[7]. For a photocatalyst to achieve high efficiency, its band gap should be around 2.0 eV, whereas the position of the band edges should be consistent with the redox potential of water[11]. A way to reduce the band gap is doping, with nitrogen (N) atom being a particularly promising p-type dopant[3,12].

Hydrogen (H) is a small atom so it can diffuse easily in inorganic compounds occupying interstitial sites. It does not induce significant structural expansion, can modify the band gap, enhance the photocatalytic activity[13], induce insulator-to-conductor transitions[14], provide free electrons[15], and interact with intrinsic defects such as oxygen vacancies[16]. H can be introduced in TiO$_2$ during synthesis or by immersion in water[12]. Interestingly, previous theoretical studies have shown that hydrogen can substitute for oxygen (termed as substitutional H, H$_O$) leading to n-type conductivity[17,18]. H doping has recently been established as an effective strategy for improving the capacitive properties of TiO$_2$ for application in supercapacitors[19]. Additionally, the emergence of a highly H doped TiO$_2$ (black titania) nanomaterial has triggered world-wide research interest, because of its substantially enhanced solar absorption and improved photocatalytic activities[20]. Notably, an effective way to achieve H doping

[1]National Center for Scientific Research Demokritos, Institute of Nanoscience and Nanotechnology (INN), 15310, Agia Paraskevi, Athens, Greece. [2]Faculty of Engineering, Environment and Computing, Coventry University, Priory Street, Coventry, CV1 5FB, United Kingdom. [3]Department of Physics, University of Patras, 26504, Patras, Greece. [4]Department of Chemical Engineering, University of Patras, 26504, Patras, Greece. [5]Cavendish Laboratory, University of Cambridge, Cambridge, CB3 0HE, United Kingdom. [6]Department of Physics & Centre for Plastic Electronics, Imperial College, London, SW7 2AZ, United Kingdom. [7]Department of Materials, Imperial College, London, SW7 2AZ, United Kingdom. Correspondence and requests for materials should be addressed to M.V. (email: m.vasilopoulou@inn.demokritos.gr) or A.C. (email: alexander.chroneos@imperial.ac.uk)

of TiO$_2$ is by subjecting it to post-annealing in a reducing environment i.e. forming gas, a 90:10 per volume mixture of nitrogen:hydrogen, which, however, indicates that simultaneous N and H codoping is possible in this case.

On the other hand, organic solar cells (OSCs) have attracted growing attention over the past decades because of their advantages in fabricating renewable, low cost, lightweight, flexible and large size light harvesting solar cells[21,22]. TiO$_2$ has been recognized as a promising electron transport layer (ETL) used to enhance the electron extraction efficiency in OSCs due to its adequate electron mobility, excellent optical transparency, and solution-based fabrication[23-25]. However, there are limitations in increasing OSCs efficiency by using as-deposited TiO$_2$ resulting from its low n-type conductivity which hampers efficient electron transport towards cathode contact and from high recombination rates of photogenerated electron-hole pairs through trap states present at the metal oxide surface[26,27]. To overcome these limitations and produce efficient metal oxide electron transport layer modification of TiO$_2$ has been developed through UV irradiation[28,29] which, however, may have a degradation effect thus hindering the device lifetime[30]. It would, therefore, be highly desirable to develop appropriate n-type doped TiO$_2$-based electron transport materials to boost the efficiency of OSCs and of related devices.

Recently, our group demonstrated the beneficial effect of H doping of zinc oxide (ZnO), which represents one of the commonly used electron transport materials in OSC technology[31,32]. However, the possible effectiveness of H as well as of N doping of TiO$_2$ used as ETLs in OSCs has not been demonstrated thus far. Moreover, the investigation of possible interaction of H and N dopants to reveal if simultaneous codoping of TiO$_2$ is possible is of high priority since the common reducing environment of TiO$_2$ contains both potential dopants. Here, we explore, **from both theoretical and experimental points of view**, the influence of H and N doping as well as of N, H codoping of anatase TiO$_2$ for application in OSCs. We show that while N causes p-type doping since it creates deep-lying intergap states that act as recombination centers which are detrimental for the device performance, H doping and, especially, N, H codoping cause n-type doping and, therefore, can be effective ways to increase the electron conductivity and passivate surface dangling bonds of TiO$_2$ leading to high-efficiency organic photovoltaics. In particular, inverted OSC devices based on photoactive blends of poly(3-hexylthiophene) (P3HT) with indene-C$_{60}$ bisadduct (IC$_{60}$BA) substantially enhanced their photovoltaic performance reaching power conversion efficiency (PCE) values of 6.51% and 6.58%, respectively, when using the H-doped and N, H-codoped TiO$_2$ ETLs. This represents an increase in performance by 34% and 35%, respectively, over the reference cells comprising an unmodified TiO$_2$ layer (4.87%). On the contrary, N doping of TiO$_2$ resulted in a decreased efficiency of 4.46% which represents an 8% efficiency drop as compared to the reference cell.

Results and Discussion

Theoretical results and discussion. TiO$_2$ has three polymorphs namely rutile, anatase and brookite. Both rutile and anatase are tetragonal with space groups P4$_2$/mnm and I4/amd respectively[33,34]. The lattice parameters of anatase TiO$_2$ are calculated at a $=$ 3.806 Å and c $=$ 9.724 Å in excellent agreement with the experimental neutron diffraction results (a $=$ 3.782 Å and c $=$ 9.502 Å)[33] and theoretical results (a $=$ 3.729–3.801 Å and c $=$ 9.480–9.818 Å)[34].

Although anatase and rutile have the same chemical composition, they differ in the coordination environments (i.e. chemical bonding) and this leads to different ionization potentials and chemical affinities[35]. Interestingly, in a recent report Luttrell *et al*[36]. studied epitaxial TiO$_2$ films to consider why anatase is a better photocatalyst as compared to rutile. This study determined that charge carriers that were excited deeper in the bulk contributed more to surface reaction in anatase as compared to rutile[36]. Considering this, the present study will focus on H and N defects in bulk anatase discussing wherever appropriate, recent DFT results concerning the anatase TiO$_2$ surface[37]. It is calculated using DFT that atomic hydrogen can be a substitutional defect occupying oxygen sites (referred to as H$_O$). This is in agreement with the present experimental results which identified only Ti^{4+} states (as discussed in the section referred to the synthesis of TiO$_2$ materials) and previous DFT studies[38]. Additionally, we considered interstitial hydrogen (H$_i$) and developed an algorithm to track the minimum energy interstitial sites using an extensive search. We calculate that H$_i$ resides 0.99 Å from the nearest oxygen atom (Fig. 1(a)). This is in agreement with previous DFT results[39].

Next, the electronic density of states (DOS) for anatase TiO$_2$ was calculated in order ito understand the electronic structure and nature of the band edge wavefunctions (Fig. 2(a)). The valence band edge of the material is dominated by O 2p, and the conduction band edge is formed from Ti 3d orbitals. The band gap is calculated to be 3.1 eV in agreement with the experimentally measured one (3.2 eV). Adding H$_i$ atoms to form multi-hydrogen clusters is energetically unfavourable (for example in the H$_i$H$_i$ pair the atoms repel each other with 1.14 eV). DOS reveal that the introduction of H leads only to a small band gap narrowing (refer to Fig. 2(b)) consistently with the experimental results shown below.

The introduction of nitrogen was considered at both a Ti site (N$_{Ti}$) or as an interstitial (N$_i$, refer to Fig. 1(b)). For N$_i$ a density of new states (refer to Fig. 2(c)) is observed above the valence band maximum, VBM (i.e. p-type doping); this is attributed to the N 2p states lying just above the O 2p states.

In codoped anatase it should be expected that N and H defects can interact. Here we have performed an extensive investigation of the different possibilities that the interstitial and/or substitutional hydrogen and nitrogen defects can associate. Figure 1(c–e) represents the N$_i$H$_i$, N$_i$H$_O$ and N$_{Ti}$H$_i$ defect pairs. The N$_i$H$_i$ defect pair is bound ($-$0.33 eV) when the two interstitials are close at N-H $=$ 1.05 Å (Fig. 1(c)) as compared to when the N-H distance is 8.07 Å. The N$_i$H$_O$ is calculated to have a binding energy of $-$3.77 eV (energy difference between configurations being at N-H $=$ 0.93 Å and N-H $=$ 7.96 Å), however, its concentration will be limited by the number of available oxygen vacancies (as there as required for H$_O$ to form). Therefore, although the majority of oxygen vacancies should be occupied by atomic hydrogen[18,32], the concentration of N$_i$H$_O$ will depend upon the growth conditions. Finally, the N$_{Ti}$H$_i$ defect is bound with $-$1.45 eV (energy difference between configurations being at N-H $=$ 2.88 Å and N-H $=$ 10.87 Å). In essence, N$_{Ti}$ defect will capture migrating H$_i$, but again this defect will require Ti vacancies to form in the first place.
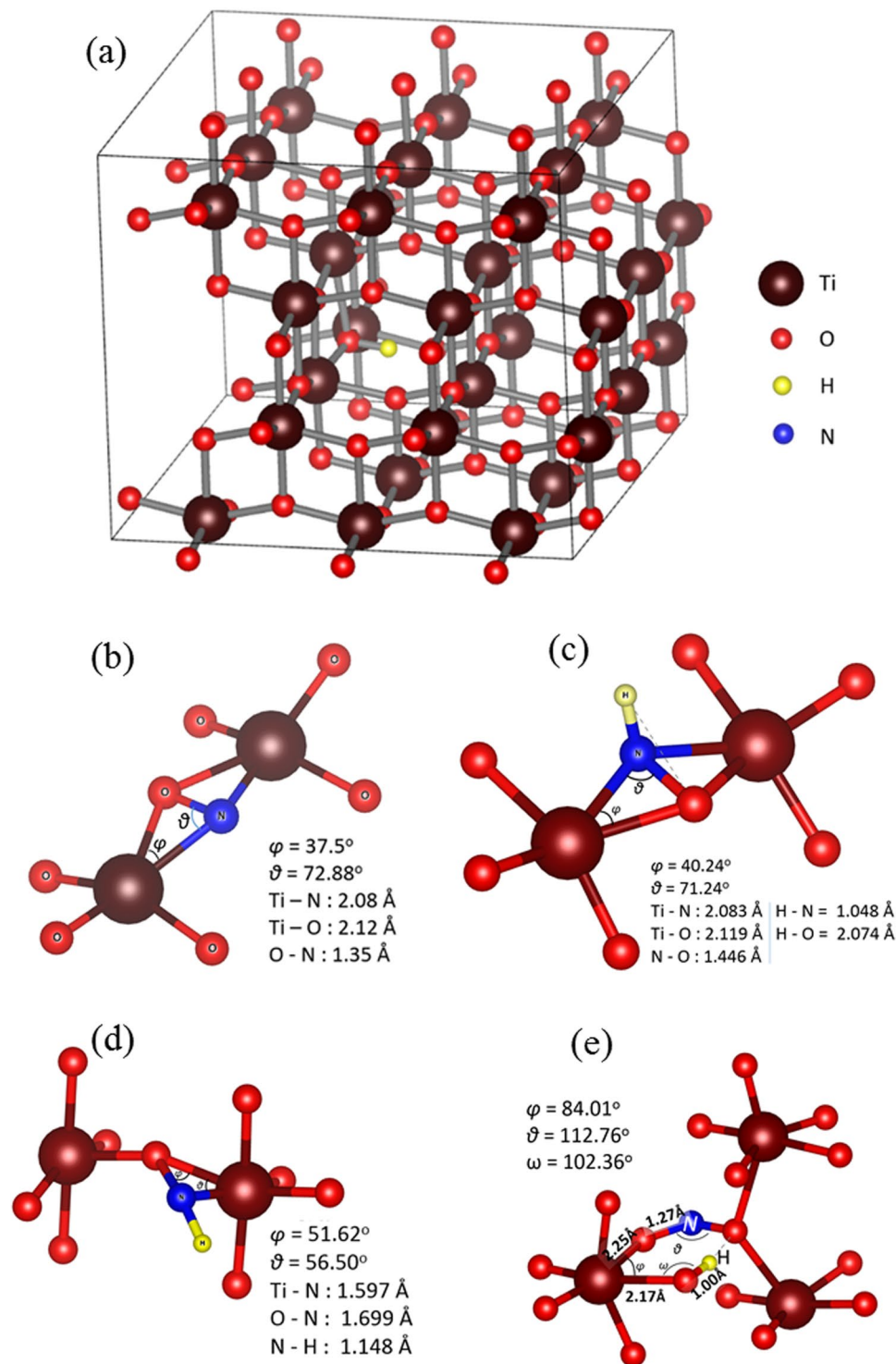
Figure 1. The structure of minimum energy defects in anatase. (**a**) H_i in the supercell, (**b**) the N_i, (**c**) N_iH_i (**d**) N_iH_O and (**e**) $N_{Ti}H_i$.

The DOS reveal that the N_iH_O and $N_{Ti}H_i$ defects (Fig. 2(e–f)) introduce levels at about 1.05 eV and 0.75 eV below the conduction band minimum, CBM. More importantly, N_iH_O defect introduces a pronounced density of states above the VBM resulting in undesirable p-type doping. These deep levels, in essence, may act as recombination centers of photo-excited electron-hole pairs and consequently can lower the efficiency of OSCs using TiO_2 ETLs. Therefore, H,N codoped TiO_2 should be grown under O-rich conditions (to provide a stoichiometric TiO_2 as the starting material) to avoid the formation of oxygen vacancies and thus N_iH_O defects.
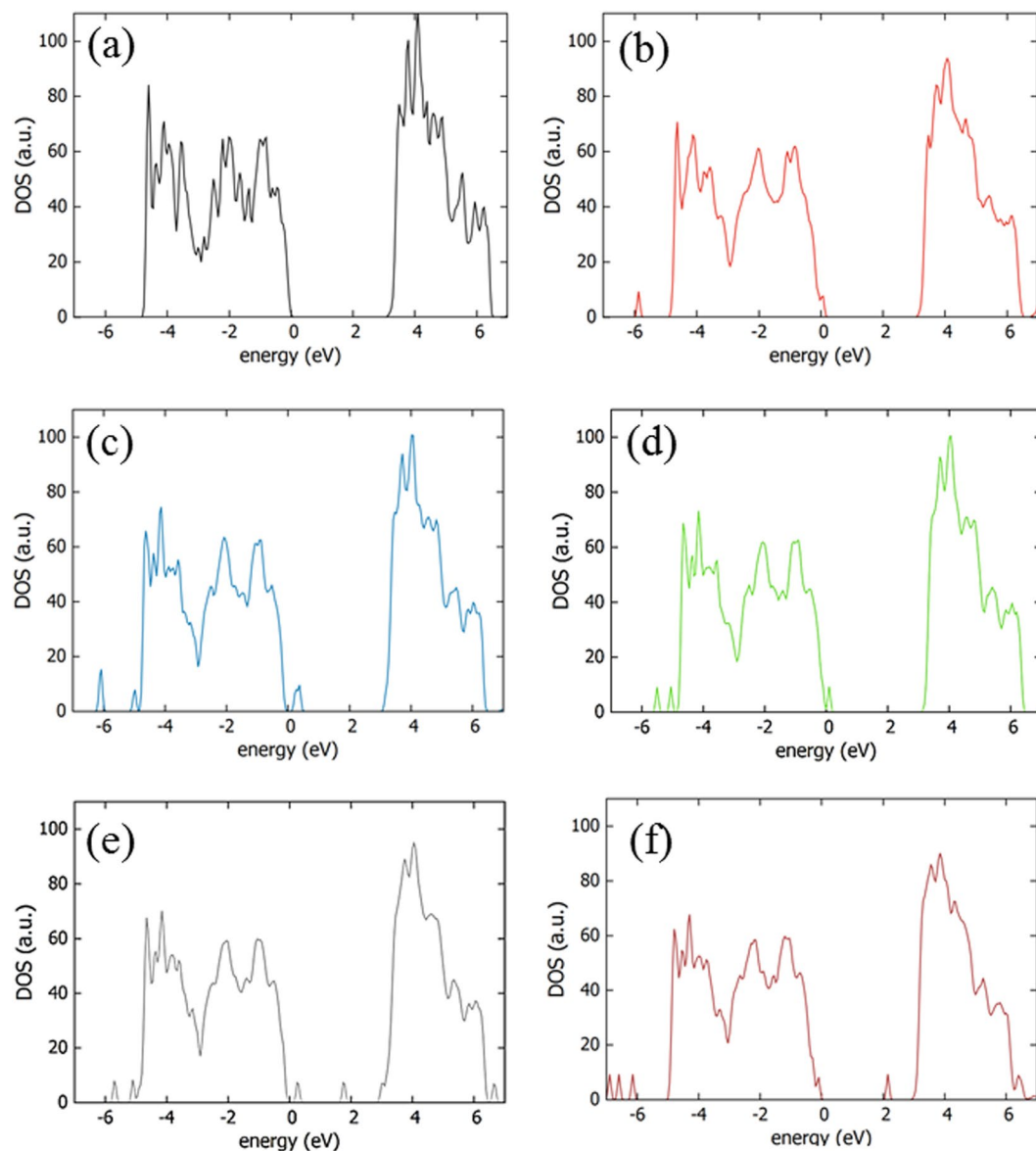
Figure 2. DOS of (**a**) undoped supercell, (**b**) H_i, (**c**) the N_i, (**d**) N_iH_i (**e**) N_iH_O and (**f**) $N_{Ti}H_i$ defects of TiO_2.

Synthesis and characterization of H and N doped and codoped TiO₂ materials.   Solution-processed anatase TiO_2 films were converted into H-doped (referred to as TiO_2:H), N-doped (referred to as TiO_2:N), or codoped (referred to as TiO_2:H,N) TiO_2 films by annealing at 550 °C in N_2, H_2, or in forming gas, respectively. In Fourier transform infra-red (FTIR) transmittance spectra (refer to Fig. S1, Supporting Information) taken in the above films exhibiting the same thickness of ~40 nm (refer to Fig. S2), apart from a broad band at the lower wave-numbers which is due to Ti-O bonds, the spectral features due to defect species are negligible; however, hydrogen and forming gas annealing seems to increase the intensity of the broad peak at 3000–3600 cm^{-1} in the region were stretching of hydroxyl group ν(OH) appears which is an indication for the insertion of hydrogen within the oxide lattice (i.e., H doping). This peak is decreased after annealing in nitrogen. From the analysis of FTIR spectra the incorporation of hydrogen dopants within the material after annealing in hydrogen and forming gas can be concluded; however, the content of H dopants cannot be estimated from those spectra since the contribution of water in the intensity of the peak around 3500 cm^{-1} cannot be excluded. Notably, the incorporation of hydrogen within the material causes some alteration in its crystallinity, especially in the hydrogen annealed sample (refer to Fig. S3). Moreover, TiO_2 samples exhibit very small band gap narrowing with H doping (from 3.20 to 3.14 eV) while the band gap narrowing is more pronounced with N doping (3.10 eV) (Fig. S4). N and H codoping only has a minor effect on the band gap value (3.13 eV). These results are in agreement with those obtained by Pan *et al*[12].

X-ray photoelectron spectroscopy (XPS) analysis of the surface elementary composition of the formulated materials confirms that N was detected in both samples deposited in environment containing N (Fig. S5). This observation indicates that N doping takes place after annealing in nitrogen and forming gas. Only Ti^{4+} states were identified in the starting material (Fig. S6), revealing that the as-deposited TiO_2 film is highly stoichiometric[40]. In
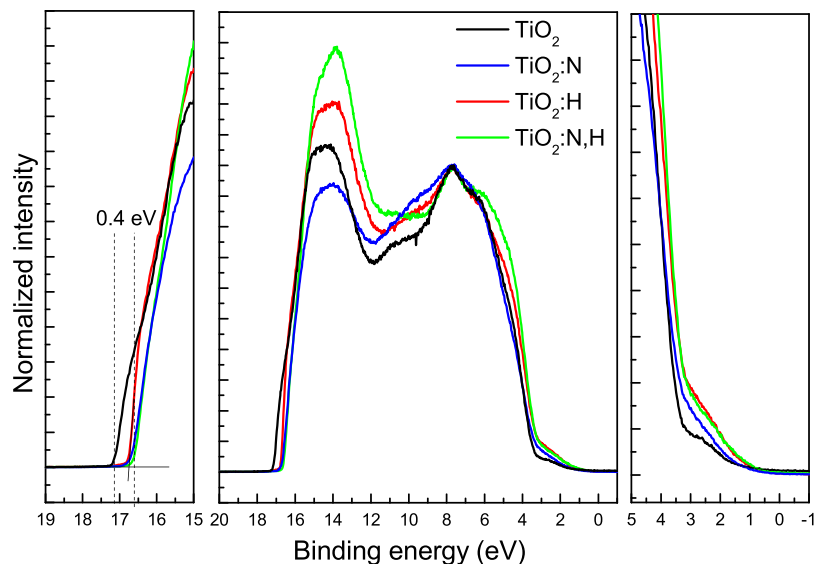
Figure 3. UPS measurements of different TiO$_2$ samples.

addition, Ti^{4+} states were also detected in the annealed samples (Fig. S6). Since we do not find localized Ti^{3+} states in our annealed samples, it can be concluded that on the sample surface there are no other Ti states. Figure S7 represents the O1s spectra of TiO$_2$ samples. The peak at binding energy 530.4 ± 0.1 eV (fittings are not included here) corresponds to O-Ti bonds in TiO$_2$. A second component is always present which is broader at binding energy 531.6 ± 0.1 eV due to Ti-OH bonds. The broadening in the O 1 s peaks of nitrogen containing samples could be due to the combination of hydroxyl groups and N-O-Ti bonds present in these samples.

The surface electronic structure of different TiO$_2$ materials was evaluated by ultra-violet photoelectron spectroscopy (UPS) measurements shown in Fig. 3, which reveal that the valence band of TiO$_2$ samples remain almost unaffected.

The valence band of the TiO$_2$ sample consists of a broad peak at about 6 eV and a narrow peak at about 8 eV, which correspond to π (non-bonding) and σ (bonding) Ti3d-O 2p orbitals[41]. An additional small peak, located at 10.6 eV, is observed in all spectra and it is more pronounced in the hydrogenated samples. This feature suggests the presence of an adsorbate such as -OH on the surface and it is correlated with the 3σ of such molecules. However, this feature is more pronounced in the spectra of samples annealed either in hydrogen or in forming gas, an indication of H doping in these cases. The VBM of TiO$_2$ is located at ~3.2 eV below the Fermi level while its work function was found equal to 4.1 eV. As its band gap is estimated to be 3.2 eV the bottom of its conduction band locates at ~4.1 eV indicating the n-type character of the TiO$_2$ film. The VBM of the doped TiO$_2$ films slightly shifts to 3.0 eV before the Fermi level while for the TiO$_2$:H and TiO$_2$:N,H samples there is an increase in the W$_F$ value by 0.3 eV which is due to the adsorbed -OH species on the surface. The work function of N containing samples is increased by 0.4 eV in comparison with the TiO$_2$ sample due to the p-type doping character of N. The results provide evidence that treatment of TiO$_2$ with hydrogen and, especially, with nitrogen results in the creation of gap states above the VBM and, concomitantly, in a decrease of the effective band gap of the semiconductor[42].

H intercalation within a metal oxide such as TiO$_2$ is expected to increase its n-type conductivity as well as to passivate surface defects[43,44]. To support this argument we next measured the current-voltage characteristics of devices with the structure glass/FTO/TiO$_2$/Al (Fig. 4(a)). The thickness of TiO$_2$ was measured at 40 nm in all cases. The significant increase in the slopes of I-V curves upon H doping and N,H codoping of TiO$_2$ witnesses the improved n-type conductivity of the latter. On the contrary, reduction of n-type conductivity is concluded from the reduced slope of the I-V curve of the TiO$_2$:N embedding diode.

The photoluminescence (PL) emission spectrum of TiO$_2$ results from the recombination of free carriers; therefore, these spectra are used to understand the effect of surface traps on photo-generated electrons and holes in TiO$_2$ samples[45]. The PL spectra of as-deposited, N and H doped and codoped TiO$_2$ samples in the wavelength range of 350–700 nm with the excitation at 325 nm are shown in Fig. 4(b). The shape of the emission spectra is very similar consisting of two broad peaks located at about 400–450 nm and at 450–600 nm, respectively. These two peaks result from surface defects of the TiO$_2$ samples. The PL peaks intensity of the H doped and N,H codoped TiO$_2$ decreases as compared to the as-deposited TiO$_2$ which is an indication of lower recombination rate of electrons and holes due to effective passivation of the surface (and bulk) defects of these samples upon H doping. Note that our doped TiO$_2$ samples retained their electrical and optical characteristics presented above when stored in air for a long period of time (data not shown).

Application of H and N doped and codoped TiO$_2$ in organic solar cells.

The configuration of the inverted polymer solar cells using TiO$_2$ electron transport layers is illustrated in Fig. 5(a), where the chemical structures of organic semiconductors (P3HT and IC$_{60}$BA) used in this study are also shown. Figures 5(b),(c) represent the J-V characteristics under full 1.5 AM simulated solar illumination and in dark, respectively, of devices using photoactive blends based on P3HT:IC$_{60}$BA with as-deposited, N and H doped and codoped TiO$_2$ ETLs, respectively.
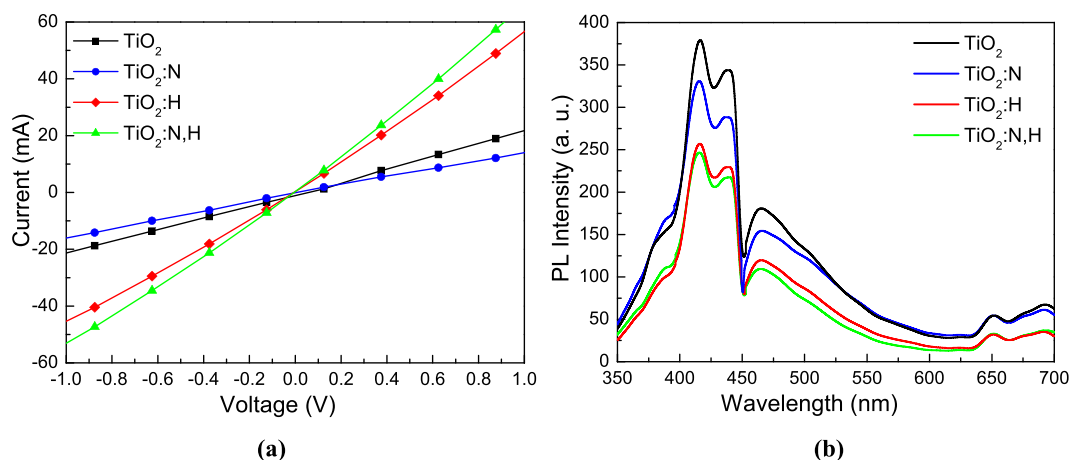
Figure 4. (**a**) Current-voltage characteristics of diodes with the structure $FTO/TiO_2/Al$ for 40 nm thick TiO_2 layers treated under different environment. (**b**) PL spectra of TiO_2 films deposited on FTO substrates with and without N and H doping and N,H codoping.
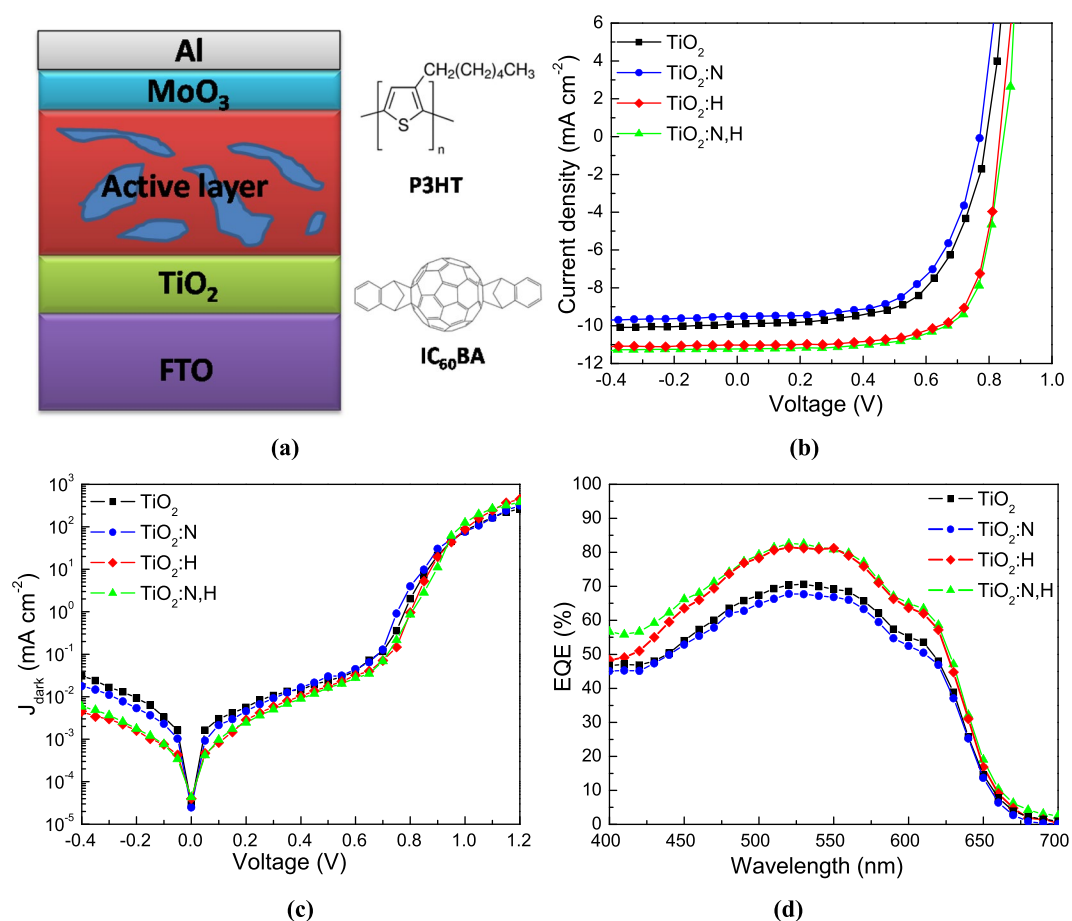

Figure 5. (**a**) The inverted organic solar cell architecture and the chemical structures of organic semiconductors used in this study. (**b**) Current density versus voltage (J-V) characteristics of $P3HT:IC_{60}BA$-based devices using as-deposited TiO_2 and doped TiO_2 films upon 1.5 AM illumination. (**c**) Dark J-V curves and (**d**) EQE measurements taken on devices embedding different TiO_2 ETLs.

The corresponding electrical output parameters of those devices are summarized in Table 1. The external quantum efficiency (EQE) characteristics of the same devices are presented in Fig. 5(d). For the reference $P3HT:IC_{60}BA$-based device with the as-deposited TiO_2 layer a PCE of 4.87% is obtained while N p-type doping of TiO_2 results in a PCE of

ETL	J_{sc}(mA cm^{-2})	$J_{sc(EQE)}$(mA cm^{-2})	V_{oc}(V)	FF	PCE(%)	R_s(Ω cm^2)	R_{sh}(Ω cm^2)
TiO$_2$	9.95 ($\pm$0.19)	9.28	0.79 ($\pm$0.01)	0.62 ($\pm$0.01)	4.87 ($\pm$0.20)	3.9	1900
TiO$_2$:N	9.50 ($\pm$0.15)	8.94	0.77 ($\pm$0.01)	0.61 ($\pm$0.01)	4.46 ($\pm$0.17)	4.7	2100
TiO$_2$:H	11.04 ($\pm$0.15)	10.70	0.83 ($\pm$0.01)	0.71 ($\pm$0.01)	6.51 ($\pm$0.16)	2.6	3900
TiO$_2$:N,H	11.19 ($\pm$0.17)	11.11	0.84 ($\pm$0.01)	0.70 ($\pm$0.01)	6.58 ($\pm$0.18)	2.7	4050

Table 1. Performance parameters of organic solar cells with the structure FTO/ETL /P3HT:IC$_{60}$BA/MoO$_3$/Al. Mean values and standard deviations were extracted from a batch of 18 identical devices.

4.46%, which is 8% lower as compared to the reference cell. On the contrary, H doping and N and H codoping result in PCEs up to 6.51% and 6.58%, respectively, representing a 34% and 35% improvement as compared to the control device. From the photovoltaic parameters presented in Table 1 becomes evident that by using TiO$_2$:H and, especially, TiO$_2$:N,H ETLs a simultaneous improvement in the open-circuit voltage (V_{oc}), short-circuit current density (J_{sc}) and fill factor (FF) of the devices is obtained. In addition, the dark J-V characteristics (shown here in semi-logarithmic scale, Fig. 5(c)) are improved in the case of TiO$_2$:H and TiO$_2$:N,H, compared to the reference and, especially, to TiO$_2$:N-based one. Importantly, the reverse saturation current density decreases significantly in the case of hydrogen containing TiO$_2$-based devices. These results suggest that H doping and N,H codoping of TiO$_2$ reduces reverse leakage and shunt current while it also facilitates electron extraction probably due to an increase of the built-in field and/or due to enhanced n-type conductivity of the metal oxide. Indeed, upon O–H bond formation, an electron is donated from the Ti–O(H)–Ti species, which results in n-type doping of the TiO$_2$ thus improving its n-type conductivity. Both reduction of the reverse saturation current and increase of the turn-on voltage contribute to the increase of the V_{oc} of the H-doped TiO$_2$-based solar cells. In addition, the devices with the TiO$_2$:H and TiO$_2$:N,H layers exhibit significantly reduced series and larger shunt resistances (refer to Table 1) verifying the overall higher quality of the corresponding diodes and explaining the enhanced J_{sc} and FF obtained in these devices. The large improvement in J_{sc} is further supported by the external quantum efficiency (EQE) measurements (refer to Fig. 5(d)). In addition, the EQE spectra of the devices were integrated from 300 to 800 nm and $J_{sc(EQE)}$ values were calculated from the integration and listed in Table 1. Notably, these values are quite consistent with the J_{sc} obtained from J–V characteristics (especially for the devices with the H doped and N,H codoped TiO$_2$) under illumination indicating the reliability of the measured J_{sc}.

Similar efficiency enhancement was obtained in organic solar cells using blends of P3HT donor with [6,6]-phenyl-C$_{70}$butyric acid methyl ester (PC$_{70}$BM) acceptor (Fig. S8) thus proving the universality of the present approach. From these results, it becomes evident that H doping of TiO$_2$, especially in the presence of nitrogen defects (i.e. N,H codoping), is an effective way to significantly improve the operational characteristics and overall performance of OSCs using TiO$_2$ ETLs while a simple nitrogen doping may negatively affect the device performance. According to our theoretical predictions and experimental results one should argue that, the presence of interstitial nitrogen (N$_i$) within the material may be beneficial for the incorporation of the non-bonded hydrogen atoms via the formation of N$_i$H$_i$ bonds thus suppressing the p-type character of N doping while simultaneously increasing the amount of H dopants in TiO$_2$.

To shed more light on the mechanisms responsible for enhanced device performance when using H doped and N,H codoped TiO$_2$ ETLs we next constructed the energy level diagram (based on UPS and absorption measurements) of various interfaces before contact (considering vacuum level alignment) at the cathode side of the device. From Fig. 6(a) it becomes evident that in all cases the lowest unoccupied molecular orbital (LUMO) of IC$_{60}$BA acceptor lies above the conduction band minimum of TiO$_2$ which indicates that electron extraction occurs via transport of electrons through the conduction band of TiO$_2$. In the n-type hydrogen-doped oxides (TiO$_2$:H and TiO$_2$:N,H) the increase of electron conductivity highly facilitates electron extraction. However, p-type doping of TiO$_2$:N sample causes the filling of localized states lying above the VBM as predicted by DFT calculations. Figure 6(b) shows that these localized states are probably aligned with the highest occupied molecular orbital (HOMO) of P3HT. As a result, after photoexcitation of P3HT through light absorption a high hole recombination rate is expected at the TiO$_2$:N/P3HT interface which significantly suppresses the device photocurrent. Note that surface states of TiO$_2$ arising from oxygen vacancies have also been proven to act as recombination centers thus deteriorating the device current and V_{oc}[30]. Passivation of such defect states via hydrogen doping and codoping is expected to be beneficial for electron extraction/collection and overall device performance. Based on the above, one should also conclude that N$_i$H$_i$ defects are rather formed in the codoped oxide because N$_i$H$_O$ and N$_{Ti}$H$_i$ are predicted to introduce deep level states, exactly as N$_i$ does, which are expected to deteriorate the device performance which was not observed in our devices embedding N,H codoped TiO$_2$.

To further elucidate the effect of N and H doping and codoping of TiO$_2$ on the optoelectronic properties of the P3HT:IC$_{60}$BA-based OSCs, we examined the charge transport properties by measuring electron-only devices with the structure: FTO/TiO$_2$/P3HT:IC$_{60}$BA/Al. The J-V characteristics are shown in semi-logarithmic plots in Fig. 7(a) and reveal a substantial increase in electron current after the insertion of H dopants in TiO$_2$. This improvement in electron current density can be attributed to the significant passivation of surface defect states as well as to increase of n-type conductivity of TiO$_2$ upon H doping and is further improved in the case of N,H codoping.

In addition, as shown in Fig. 7(b), where a log-linear plot of V_{oc} as a function of the light intensity is presented, the slope values of V_{oc} were decreased from 1.14 to 1.07 and 1.05 k_BT/q upon H doping and N,H codoping, where k_B is Boltzmann's constant, T is the absolute temperature, and q is the elementary charge. On the contrary, the slope increases to 1.21 k_BT/q upon N doping of TiO$_2$ ETL. This confirms that the insertion of H dopants into the
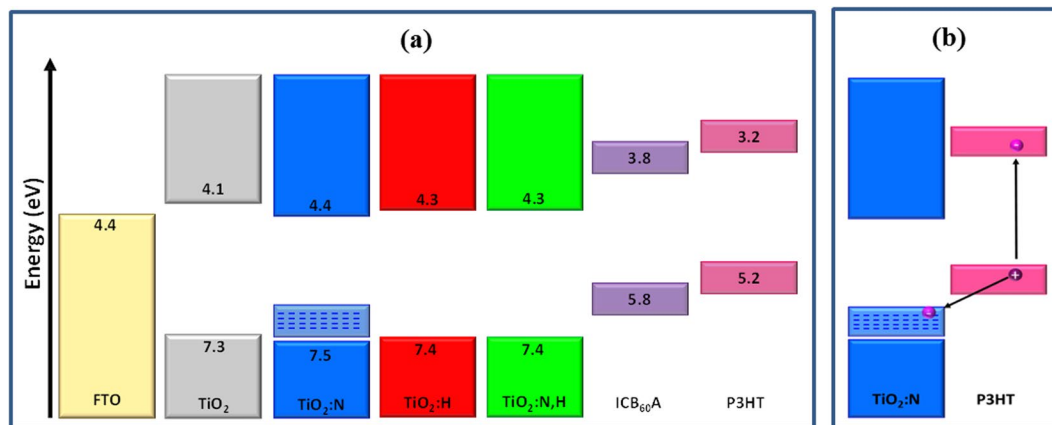
Figure 6. (a) Energy level diagram of cathode interfaces with different TiO₂ ETLs. (**b**) Illustration of possible hole recombination process occurring at the TiO₂:N/P3HT interface.
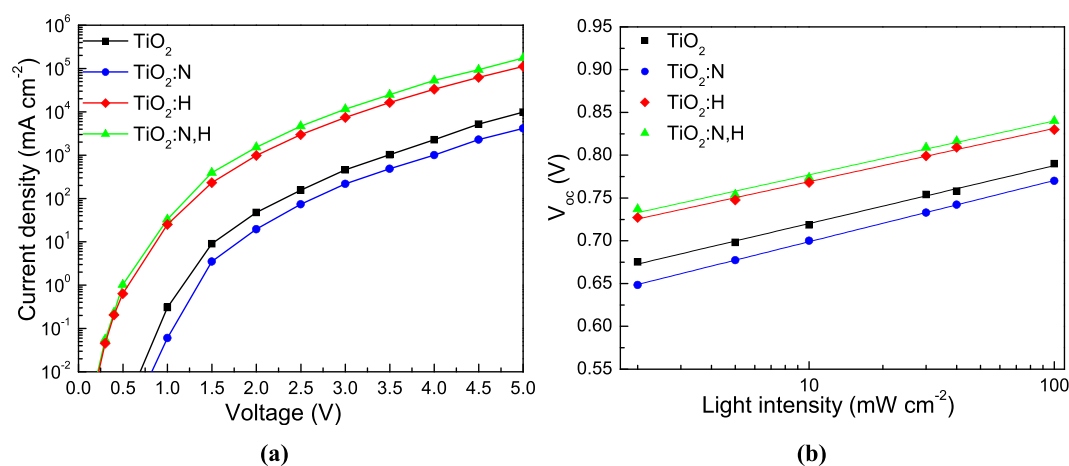

Figure 7. (**a**) Current density-voltage (J−V) curves (measured in dark) in semi-log plot obtained in electron-only devices with the structure: glass/FTO/TiO₂/P3HT:IC₆₀BA/Al where TiO₂ ETLs are as-deposited N, H or N,H co-doped. (**b**) Dependence of V_{oc} on 1.5 AM illuminated light intensity of P3HT:IC₆₀BA-based organic solar cells using different TiO₂ ETLs.

TiO₂ lattice significantly reduced trap-assisted recombination at open circuit by passivating surface defects on TiO₂, leading to an enhanced electron collection (and consequently, J_{sc}), FF and PCE values[46].

Apart from the increased efficiency the high long term stability under ambient air of organic solar cells is highly desirable and was verified in the case of H doped and N,H codoped TiO₂ embedding devices (refer to Fig. 8). The improved stability of the doped samples can be partly explained by the fact that H dopants terminate dangling bonds preventing adsorption of oxygen and moisture on the TiO₂ surface[47]. Note that the devices were intentionally un-encapsulated so that they were exposed to ambient conditions (moisture and oxygen) throughout the aging study.

Finally, to evaluate our approach in cases where lower thermal budget is necessary, we fabricated P3HT:IC₆₀BA-based OSCs using TiO₂ ETLs post-annealed at 300 °C for 30 min to obtain H, N, or N,H codoping (refer to Fig. S9). It is observed that annealing in hydrogen containing environment induces significant enhancement in the device performance as compared to the reference cell while nitrogen annealing of TiO₂ causes a small reduction in the device photocurrent and FF. Those results represent an indication that the intercalation of significant amount of H dopants in TiO₂ is an effective way for boosting its electron transport capability for application in organic photovoltaics and related cells. Note that, our group has recently demonstrated the beneficial effect of H doping of ZnO (annealed at 300 °C in hydrogen environment) for organic solar cells application[32]. Based on the present results, an extensive study regarding N, H doping and N,H codoping of ZnO and influence on organic optoelectronics seems necessary and is currently carried out.

In the present study, H and N doped and codoped anatase TiO₂ was systematically investigated using a range of experimental techniques and DFT calculations. DFT calculations reveal that the N_iH_i, N_iH_O and $N_{Ti}H_i$ defects are bound, although the latter two defects require vacancies and this may hinder their formation. Conversely, H_i do not bind together to form extended H clusters. It is therefore expected that in codoped anatase there will be
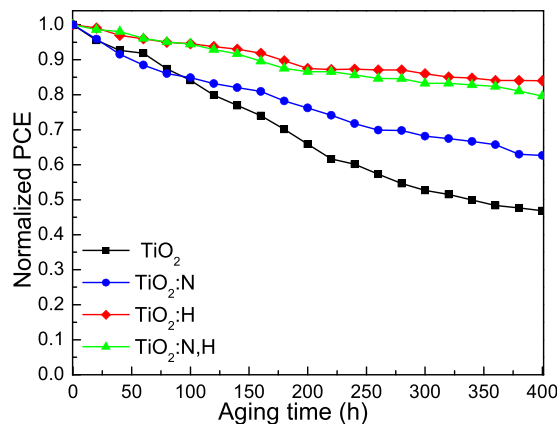
Figure 8. Stability measurements in ambient air: Variation of normalized PCE over a period of 400 hours for P3HT:IC$_{60}$BA-based devices using of TiO$_2$ ETLs with and without N, H doping and N,H codoping.

a significant concentration of N$_i$H$_i$ and possibly N$_i$H$_O$ and N$_{Ti}$H$_i$ provided that there exist vacancies so that H$_O$ and N$_{Ti}$ may form. The experimental results indicate that the formation N$_i$H$_i$ is more probable since they do not create deep defect states which are expected to act as hole recombination centers. H doping and N, H codoping both boost the efficiency as well as the ambient stability of organic solar cells based on P3HT:IC$_{60}$BA. H doping and codoping with N offer several advantages including increase electron conductivity and less density of surface traps and defects at grain boundaries. The combined effects resulted in a remarkable enhancement of V$_{oc}$, J$_{sc}$ and FF in H doped N,H codoped TiO$_2$-based OSCs.

Methods

Titanium Oxide Layer Preparation. FTO-coated glass (Pilkington TEC 15, <15 Ohms/sq) was cleaned by sonication in detergent solution (Hellmanex III, Hellma Analytics), water and ethanol, followed by treatment in an oxygen plasma for 5 min. A solution of 13 μL concentrated aqueous HCl in 5 mL of dry isopropanol was slowly added to a stirred solution of titanium isopropoxide (711 mg, 2.5 mmol) in 5 mL of dry isopropanol. The cleaned substrates were spin-coated at 2000 rpm with this titania precursor solution and immediately placed on a hotplate at 150 °C. Subsequently, the samples were calcinated at 500 °C for 45 min (1 h ramp). N and H doped and codoped TiO$_2$ were obtained after annealing in nitrogen, hydrogen and forming gas environment at 550 °C for 1 hour. The annealing was made in a home-made furnace equipped with a quartz chamber with a graphite susceptor on which samples were placed. The susceptor was radiatively heated by three tungsten-halogen lamps of 1000 W each. The temperature of the susceptor (and therefore of the samples on it) was controlled with an automatic temperature control system, which was receiving feedback from a thermocouple positioned in a hole on the graphite and was controlling the power of the lamps. After loading samples, the chamber was evacuated down to 2 10^{-2} Torr. Then a nitrogen stream was allowed to flow through it to maintain a pressure of 0.1 Torr and the temperature was raised to the desired point (550 °C). After the preset temperature was reached, the chamber was evacuated again down to 2 10^{-2} Torr and a stream of the doping gas (hydrogen or forming gas or pure nitrogen) was introduced in it at a pressure of 1 Torr. At the end of the annealing the chamber was evacuated from the doping gas, the heating lamps were turned off and the samples were left to cool down to 70 °C under 0.1 Torr of nitrogen.

Device Fabrication. Organic solar cells were fabricated on 40 nm thick TiO$_2$ films (as-deposited or doped), which served as the electron transport layers, deposited on FTO coated glass substrates, as described above. The active layer consisted of a P3HT:IC$_{60}$BA blend (17 mg ml^{-1} for P3HT, 17 mg ml^{-1} for IC$_{60}$BA in 1,2-dichlorobenzene). After spin coating at 800 rpm for 30 sec the photoactive layers were left to dry for 30 min and then annealed at 150 °C for 15 min. Note that all depositions and thermal annealing treatments were carried out in the inert environment of an argon filled glove-box. Then, an approximately 20 nm-thick under-stoichiometric molybdenum oxide (MoO$_3$) layer was deposited on top of the active layer, using a previously reported method, to serve as the hole transport/extraction material[48,49]. The devices were completed with a 150 nm thick aluminium anode, deposited in a dedicated thermal evaporator at a pressure of 10^{-6} Torr through a shadow-mask, which defined the device active area to be equal to 12.56 mm^2. The devices were then measured in air at room temperature without additional encapsulation. P3HT was purchased from Rieke metals and IC$_{60}$BA was purchased from Solenne.

Measurements and Instrumentation. XPS and UPS were recorded by Leybold EA-11 electron analyzer operating in constant energy mode at pass energy of 100 eV and at a constant retard ratio of 4 eV for XPS and UPS, respectively. All binding energies were referred to the C 1 s peak at 284.8 eV of surface adventitious carbon. The X-ray source for all measurements was an unmonochromatized Mg Kα line at 1253.6 eV (12 keV with 20 mA anode current). The valence band spectra of TiO$_2$ samples were evaluated after recording the UPS spectra of approximately 40 nm thick films deposited on an FTO substrate. For the UPS measurements, the He I (21.22 eV) excitation line was used. A negative bias of 12.22 V was applied to the samples during UPS measurements in order to separate secondary electrons originating from sample and spectrometer and to estimate the absolute

work function value from the high BE cut-off region of the UPS spectra. The analyzer resolution is determined from the width of the Au Fermi edge to be 0.16 eV. Absorption measurements were taken using a Perkin Elmer Lambda 40 UV/Vis spectrophotometer. FTIR transmission spectra were obtained on a Bruker Tensor 27 spectrometer (at 4 cm^{-1} resolution, 128 scans). Film thicknesses were measured with an Ambios XP-2 profilometer. Photoluminescence measurements on TiO$_2$ were carried out using a Horiba Jobin-Yvon iHR320 Spectrometer with a He–Cd laser (325 nm) as excitation source. X-ray diffraction (XRD) measurements were performed using a Siemens D500 diffractometer with Cu-Ka radiation. Current density-voltage characteristics of the fabricated solar cells were measured with a Keithley 2400 source-measure unit. Cells were illuminated with a Xe lamp and an AM 1.5 G filter to simulate solar light illumination conditions with an intensity of 100 mW/cm^2 (1 sun), as recorded with a calibrated silicon photodiode. To accurately define the active area of all devices, we used aperture masks during the measurements with their area equal to those of the Al contacts (12.56 mm^2). EQE measurements were carried out using an Autolab PGSTAT-30 potentiostat, with a 300 W Xe lamp in combination with an Oriel 1/8 monochromator for dispersing the light in an area of 0.5 cm^2. A Thorlabs silicon photodiode was used for the calibration of the spectra. All measurements were performed in air.

Computational methodology. The calculations were performed in thermally stable anatase TiO$_2$ using the plane wave DFT code CASTEP[50,51]. Exchange and correlation interactions were modelled with the corrected density functional of Perdew, Burke and Ernzerhof (PBE)[52] in the generalized gradient approximation (GGA), with ultrasoft pseudopotentials[53]. Spin polarized calculations with the inclusion of the Hubbard U contribution were used to account for the strong Coulombic interaction of the localised electrons of the 3d orbitals of Ti. The U value was set to 8.2 eV as this brings the band gap close to the experimental one in agreement to the study of Kiarii et al[54]. The plane wave basis set was set to a cut-off of 480 eV, in conjunction with a $7 \times 7 \times 7$ Monkhorst-Pack (MP)[55] k-point grid and a 108-atomic site supercell. The calculations were under constant pressure conditions. The minimum energy interstitial sites and interstitial clusters were calculated by using an extensive search of all the possible combinations. We adopted and reported only the minimum energy configurations. The calculated DOS values are given in Fig. 2 with the Fermi level set at 0 eV.

References

1. Fujishima, A. & Honda, K. Electrochemical photolysis of water at a semiconductor electrode. *Nature* **238**, 5358 (1972).
2. Gratzel, M. Photoelectrochemical cells. *Nature* **414**, 338–344 (2001).
3. Asahi, R., Morikawa, T., Ohwaki, T., Aoki, K. & Taga, Y. Visible-light photocatalysis in nitrogen-doped titanium oxides. *Science* **293**, 269–271 (2001).
4. Khan, S. U. M., Al-Shahry, M. & Ingler, W. B. Efficient photochemical water splitting by a chemically modified n-TiO$_2$. *Science* **297**, 2243–2245 (2002).
5. Russo, S. P., Grey, I. E. & Wilson, N. C. Nitrogen/hydrogen codoping of anatase: A DFT study. *J. Phys. Chem. C* **112**, 7653–7664 (2008).
6. Yang, H. G. *et al*. Anatase TiO$_2$ single crystals with a large percentage of reactive facets. *Nature* **453**, 638–641 (2008).
7. Gai, Y., Li, J., Li, S.-S., Xia, J.-B. & Wei, S.-H. Design of narrow-gap TiO$_2$: A passivated codoping approach for enhanced photoelectrochemical activity. *Phys. Rev. Lett.* **102**, 036402 (2009).
8. Dou, L. *et al*. Tandem Polymer Solar Cells Featuring a Spectrally Matched Low-Bandgap Polymer. *Nat. Photonics* **6**, 180–185 (2012).
9. Sivula, K. & van de Krol, R. Semiconducting materials for photoelectrochemical energy conversion. *Nat. Mater. Rev.* **1**, 15010 (2016).
10. Zhu, J. *et al*. Intrinsic defects and H doping in WO$_3$. *Sci. Rep.* **7**, 40882 (2017).
11. Khaselev, O. & Turner, J. A. A monolithic photovoltaic-photoelectrochemical device for hydrogen production via water splitting. *Science* **280**, 425 (1998).
12. Pan, H., Zhang, Y.-W., Shenoy, V. B. & Gao, H. Effects of H-, N-, and (H, N)-doping on the photocatalytic activity of TiO$_2$. *J. Phys. Chem. C* **115**, 12224–12231 (2011).
13. Chen, X., Liu, L., Yu, P. Y. & Mao, S. S. Increasing solar absorption for photocatalysis with black hydrogenated titanium dioxide nanocrystals. *Science* **331**, 746–750 (2011).
14. Kobayashi, Y. *et al*. An oxyhydride of BaTiO$_3$ exhibiting hydride exchange and electronic conductivity. *Nat. Mater.* **11**, 507–511 (2012).
15. Ma, X., Dai, Y., Yu, L. & Huang, B. Noble-metal-free plasmonic photocatalyst: Hydrogen doped semiconductors. *Sci. Rep.* **4**, 3986 (2014).
16. Gerosa, M., Valentin, C. D., Onida, G., Bottani, C. E. & Pacchioni, G. Anisotropic effects of oxygen vacancies on electrochromic properties and conductivity of γ-monoclinic WO$_3$. *J. Phys. Chem. C* **120**, 11716–11726 (2016).
17. Van de Walle, C. G. & Neugebauer, J. Universal alignment of hydrogen levels in semiconductors, insulators and solutions. *Nature* **423**, 626–628 (2003).
18. Janotti, A. & de Walle, Van C. G. Hydrogen multicentre bonds. *Nature Mater.* **6**, 44–47 (2007).
19. Lu, X. *et al*. Hydrogenated TiO$_2$ nanotube arrays for supercapacitors. *Nano Lett.* **12**(3), 1690–1696 (2012).
20. Liu, X. *et al*. Progress in Black Titania: A new material for advanced photocatalysis. *Adv. Energy Matter.* **6**, 1600452 (2016).
21. Yu, G., Hummelen, J., Wudl, F. & Heeger, A. J. Polymer photovoltaic cells: Enhanced efficiencies via a network of internal donor-acceptor heterojunctions. *Science* **270**, 1789–1791 (1995).
22. Halls, J. J. M. *et al*. Efficient photodiodes from interpenetrating polymer networks. *Nature* **376**, 498–500 (1995).
23. Sun, Y. M., Seo, J. H., Takacs, C. J., Seifter, J. & Heeger, A. J. Inverted polymer solar cells integrated with a low-temperature-annealed sol-gel-derived ZnO film as an electron transport layer. *Adv. Mater.* **23**, 1679–1683 (2011).
24. Liao, S.-H., Jhuo, H.-J., Cheng, Y.-S. & Chen, S.-A. Fullerene derivative-doped zinc oxide nanofilm as the cathode of inverted polymer solar cells with low-bandgap polymer (PTB7-Th) for high performance. *Adv. Mater.* **25**, 4766–4771 (2013).
25. Chen, S. *et al*. Thermo-cleavable fullerene materials as buffer layers for efficient polymer solar cells. *J. Mater. Chem. A* **1**, 11170–11176 (2013).
26. Tam, K. H. *et al*. Defects in ZnO nanorods prepared by a hydrothermal method. *J. Phys. Chem. B* **110**, 20865–20871 (2006).
27. Linsebigler, A. L., Lu, G. & Yates, J. T. Jr. Photocatalysis on TiO$_2$ surfaces: principles, mechanisms, and selected results. *Chem. Rev.* **95**, 735–758 (1995).
28. Trost, S. *et al*. Overcoming the "light-soaking" issue in inverted organic solar cells by the use of Al:ZnO electron extraction layers. *Adv. Energy Mater.* **3**, 1437–1444 (2013).
29. Lin, Z., Jiang, C., Zhu, C. & Zhang, J. Development of inverted organic solar cells with TiO$_2$ interface layer by using low-temperature atomic layer deposition. *ACS Appl. Mater. Interfaces* **5**, 713–718 (2013).
30. Vasilopoulou, M. *et al*. Atomic-layer-deposited aluminum and zirconium oxides for surface passivation of TiO2 in high-efficiency organic photovoltaics. *Adv. Energy Mater.* **4**, 1400214 (2014).

31. Papamakarios, V. *et al*. Surface modification of ZnO layers via hydrogen plasma treatment for efficient inverted polymer solar cells. *ACS Appl. Matter. Interfaces* **8**, 1194–1205 (2015).
32. Polydorou, E. *et al*. Avoiding ambient air and light induced degradation in high-efficiency polymer solar cells by the use of hydrogen-doped zinc oxide as electron extraction material. *Nano Energy* **34**, 500–514 (2017).
33. Burdett, J. K., Hughbanks, T., Miller, G. J., Richardson, J. W. & Smith, J. V. Structural-electronic relationships in inorganic solids: powder neutron diffraction studies of the rutile and anatase polymorphs of titanium dioxide at 15 and 295 K. *J. Am. Chem. Soc.* **109**, 3639–3646 (1987).
34. Muscat, J., Swamy, V. & Harrison, N. W. First-principles calculations of the phase stability of TiO$_2$. *Phys. Rev. B* **65**, 224112 (2002).
35. Scanlon, D. O. *et al*. Band alignment of rutile and anatase TiO$_2$. *Nat. Mater.* **12**, 798–801 (2008).
36. Luttrell, T. *et al*. Why is anatase a better photocatalyst than rutile? Model studies on epitaxial TiO$_2$ films. *Sci. Rep.* **4**, 4043 (2014).
37. Sotoudeh, M., Hashemifar, S. J., Abbasnejad, M. & Mohammadizadeh, M. R. *Ab-initio* study of hydrogen doping and oxygen vacancy at anatase TiO$_2$ surface. *AIP Adv.* **4**, 027129 (2014).
38. Mehta, M. *et al*. Hydrogen treated anatase TiO$_2$: A new experimental approach and further insights from theory. *J. Mater. Chem. A* **4**, 2670–2681 (2016).
39. Miyagi, T., Kamei, M., Mitsuhasi, T. & Yamazaki, A. Discovery of the deep level related to hydrogen in anatase TiO$_2$. *Appl. Phys. Lett.* **88**, 132101 (2006).
40. Biesinger, M. C., Lau, L. W. M., Gerson, A. R. & Smart, R. S. C. Resolving surface chemical states in XPS analysis of first row transition metals, oxides and hydroxides: Sc, Ti, V, Cu and Zn. *Appl. Surf. Sci.* **257**, 887–898 (2010).
41. Thomas, A. G. *et al*. Comparison of the electronic structure of anatase and rutile TiO$_2$ single-crystal surfaces using resonant photoemission and x-ray absorption spectroscopy. *Phys. Rev. B.* **75**, 35105 (2007).
42. Ioannidou, E. *et al*. Correlating the properties of hydrogenated titania to reaction kinetics and mechanism for the photocatalytic degradation of bisphenol A under solar irradiation. *Appl. Catal. B Environ.* **188**, 65–76 (2016).
43. Polydorou, E., Soultati, A. & Vasilopoulou, M. Highly conductive, optically transparent, low work function hydrogen-doped boron-doped ZnO electrodes for efficient ITO-free polymer solar cells. *J. Mater. Chem. C.* **4**, 691–703 (2016).
44. Lei, Y. *et al*. Preparation and photoluminescence of highly ordered TiO$_2$ nanowire arrays. *Appl. Phys. Lett.* **78**, 1125–1127 (2001).
45. Cowan, S. R., Roy, A. & Heeger, A. J. Recombination in Polymer-Fullerene Bulk Heterojunction Solar Cells. *Phys. Rev. B* **82**, 245207 (2010).
46. Vasilopoulou, M. *et al*. Large Work Function Shift of Organic Semiconductors Inducing Enhanced Interfacial Electron Transfer in Organic Optoelectronics Enabled by Porphyrin Aggregated Nanostructures. *Nano Res.* **7**, 679–693 (2014).
47. Sánchez, J. G. *et al*. Stability study of high efficiency polymer solar cells using TiO$_x$ as electron transport layer. *Solar Energy* **150**, 147–155 (2017).
48. Kostis, I. *et al*. Effect of the oxygen sub-stoichiometry and of hydrogen insertion on the formation of intermediate bands within the gap of disordered molybdenum oxide films. *J. Phys. Chem. C* **117**, 18013–18020 (2013).
49. Vasilopoulou, M., Raptis, I., Argitis, P., Aspiotis, I. & Davazoglou, D. Polymeric electrolytes for WO$_3$-based all solid-state electrochromic displays. *Microelectron. Eng.* **83**, 1414–1417 (2006).
50. Payne, M. C., Teter, M. P., Allan, D. C., Arias, T. A. & Joannopoulos, J. D. Iterative minimization techniques for *ab initio* total-energy calculations: molecular dynamics and conjugate gradients. *Rev. Mod. Phys.* **64**, 1045 (1992).
51. Segall, M. D. *et al*. First-principles simulation: ideas, illustrations and the CASTEP code. *J. Phys. Condens. Matter* **14**, 2717 (2002).
52. Perdew, J., Burke, K. & Ernzerhof, M. Generalized gradient approximation made simple. *Phys. Rev. Lett.* **77**, 3865 (1996).
53. Vanderbilt, D. Soft self-consistent pseudopotentials in a generalized eigenvalue formalism. *Phys. Rev. B* **41**, 7892 (1990).
54. Kiarii, E. M., Govender, K. K., Ndungu, P. G. & Govender, P. P. The generation of charge carriers in semiconductors- A theoretical study. *Chem. Phys. Lett.* **678**, 167–176 (2017).
55. Monkhorst, H. J. & Pack, J. D. Special points for Brillouin-zone integrations. *Phys. Rev. B* **13**, 5188 (1976).

Acknowledgements

Author Contributions

M.V., E.P., A.S., D.D., P.A.G.P., F.A., S.K., D.T. and D.G.G. performed the experiments and N.K., S.R.G.C., and A.C. the calculations. All authors contributed to the interpretation of the results and the writing of the paper.

Additional Information

Supplementary information accompanies this paper at https://doi.org/10.1038/s41598-017-18051-0.

Competing Interests: The authors declare that they have no competing interests.

Publisher's note: Springer Nature remains neutral with regard to jurisdictional claims in published maps and institutional affiliations.